Title

Evidence for distinct rate-limiting steps in the cleavage of alkenes by carotenoid cleavage dioxygenases

Journal

Journal of Biological Chemistry, 294(27)

ISSN

0021-9258

Authors

Khadka, Nimesh
Farquhar, Erik R
Hill, Hannah E
et al.

Publication Date

2019-07-01

DOI

10.1074/jbc.ra119.007535

Peer reviewed

Evidence for distinct rate-limiting steps in the cleavage of alkenes by carotenoid cleavage dioxygenases

Received for publication, January 12, 2019, and in revised form, May 24, 2019 Published, Papers in Press, May 28, 2019, DOI 10.1074/jbc.RA119.007535

Nimesh Khadka[‡], Erik R. Farquhar[§¶], Hannah E. Hill[‡], Wuxian Shi[§¶], Johannes von Lintig[‡], and Philip D. Kiser[‡‖1]

From the [‡]Department of Pharmacology, School of Medicine, Case Western Reserve University, Cleveland, Ohio 44106, [§]National Synchrotron Light Source-II, Brookhaven National Laboratory, Upton, New York 11973, [¶]Center for Proteomics and Bioinformatics, Center for Synchrotron Biosciences, School of Medicine, Case Western Reserve University, Cleveland, Ohio 44106-4988, and [‖]Research Service, Louis Stokes Cleveland Veterans Affairs Medical Center, Cleveland, Ohio 44106

Edited by F. Peter Guengerich

Carotenoid cleavage dioxygenases (CCDs) use a nonheme Fe(II) cofactor to split alkene bonds of carotenoid and stilbenoid substrates. The iron centers of CCDs are typically five-coordinate in their resting states, with solvent occupying an exchangeable site. The involvement of this iron-bound solvent in CCD catalysis has not been experimentally addressed, but computational studies suggest two possible roles. 1) Solvent dissociation provides a coordination site for O_2, or 2) solvent remains bound to iron but changes its equilibrium position to allow O_2 binding and potentially acts as a proton source. To test these predictions, we investigated isotope effects (H_2O *versus* D_2O) on two stilbenoid-cleaving CCDs, *Novosphingobium aromaticivorans* oxygenase 2 (NOV2) and *Neurospora crassa* carotenoid oxygenase 1 (CAO1), using piceatannol as a substrate. NOV2 exhibited an inverse isotope effect ($k_H/k_D \sim 0.6$) in an air-saturated buffer, suggesting that solvent dissociates from iron during the catalytic cycle. By contrast, CAO1 displayed a normal isotope effect ($k_H/k_D \sim 1.7$), suggesting proton transfer in the rate-limiting step. X-ray absorption spectroscopy on NOV2 and CAO1 indicated that the protonation states of the iron ligands are unchanged within pH 6.5– 8.5 and that the Fe(II)–aquo bond is minimally altered by substrate binding. We pinpointed the origin of the differential kinetic behaviors of NOV2 and CAO1 to a single amino acid difference near the solvent-binding site of iron, and X-ray crystallography revealed that the substitution alters binding of diffusible ligands to the iron center. We conclude that solvent-iron dissociation and proton transfer are both associated with the CCD catalytic mechanism.

Carotenoid cleavage dioxygenases (CCDs)[2] constitute a family of nonheme iron enzymes that catalyze the cleavage of alkene bonds to form carbonyl-containing products (1–3). Carotenoids are the canonical substrates for CCDs, but some members of this family instead cleave noncarotenoid compounds such as stilbenoids (4). CCDs play crucial roles in various synthetic biological processes (5, 6). These include the formation of retinaldehyde chromophores for opsin proteins (7) and signaling molecules such as abscisic acid (8), retinoic acid (9), and strigolactones (10). Some CCDs, *e.g.* β-carotene oxygenase 2, also function as catabolic enzymes to degrade potentially toxic carotenoids (11). Despite progress made in elucidating CCD substrate specificity and biological activity, the mechanisms by which these enzymes bind their substrates and activate O_2 to achieve regioselective alkene bond cleavage remain incompletely understood.

X-ray crystal structures of *Synechocystis* sp. PCC 6803 apocarotenoid oxygenase (ACO) (12) and 9-*cis*-epoxycarotenoid dioxygenase from *Zea mays* viviparous-14 (VP14) (13) and more recent studies on stilbene-cleaving CCDs from fungi (14) and bacteria (15, 16) have revealed a conserved active-site geometry for the CCD family. The resting-state active site contains an iron cofactor coordinated by four conserved His residues (Fig. 1). Two *cis*-localized sites in the iron-coordination sphere are unoccupied by protein ligands and are potentially available for diffusible ligand binding. In all structures mentioned above except that for VP14, one of the vacant sites is partially occluded by the methyl group of a nearby Thr side chain, which prevents the metal from attaining a complete six-coordinate octahedral ligand set. The accessible site is occupied by a solvent molecule in a majority of these crystal structures, although two of them contain modeled O_2 instead (13, 15). The resting-state iron structure with four coordinating His residues and a bound solvent ligand gives the metal center a distorted square pyramidal geometry. X-ray absorption spectroscopy (XAS) and Mössbauer spectroscopy studies on the iron centers of NOV2, CAO1, and ACO further corroborated their five-coordinate geometry and established that they are all in a high-spin Fe(II) state (14).

This work was supported by National Institutes of Health Grants R01EY009339 (to P. D. K.) and R01EY020551 (to J. v. L.), Department of Veterans Affairs Grant IK2BX002683 (to P. D. K.), and Burroughs Wellcome Fund Award 1015187 (to P. D. K.). The authors declare that they have no conflicts of interest with the contents of this article. The content is solely the responsibility of the authors and does not necessarily represent the official views of the National Institutes of Health or the Department of Veterans Affairs.

This article contains Figs. S1–S8 and Tables S1 and S2.

The atomic coordinates and structure factors (codes 6N1Y, 6N20, and 6N21) have been deposited in the Protein Data Bank (http://wwpdb.org/).

[1] To whom correspondence should be addressed: Dept. of Physiology and Biophysics, School of Medicine, University of California Irvine School of Medicine, 837 Health Sciences Rd., Irvine, CA 92617. Tel.: 949-824-6954; E-mail: pkiser@uci.edu.

[2] The abbreviations used are: CCD, carotenoid cleavage dioxygenase; ACO, *Synechocystis* sp. PCC 6803 apocarotenoid oxygenase; CAO1, *N. crassa* carotenoid oxygenase 1; k_D, k_{cat} in D_2O; k_H, k_{cat} in H_2O; KIE, kinetic isotope effect; NOV2, *N. aromaticivorans* oxygenase 2; KIE, kinetic isotope effect; sKIE, solvent kinetic isotope effect; VP14, *Z. mays* viviparous-14; XANES, X-ray absorption near-edge spectroscopy; XAS, X-ray absorption spectroscopy; SSRL, Stanford Synchrotron Radiation Lightsource; PDB, Protein Data Bank; pL, negative logarithm of the lyonium ion concentration.

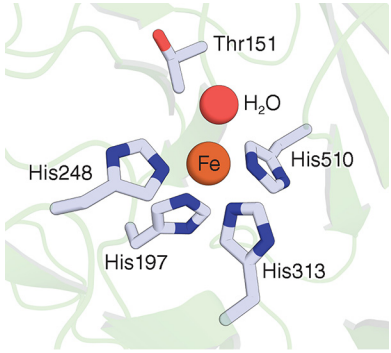

Figure 1. Resting state structure of the CAO1 active site. The iron center of CAO1, a representative stilbene-cleaving CCD, is shown in the figure. Four histidine residues (His-197, -248, -313, and -510) coordinate the Fe(II) ion with an exchangeable aquo ligand as the fifth coordinating ligand. The figure was produced using atomic coordinates deposited under PDB code 5U8X.

Crystal structures of cobalt-substituted CAO1 in complex with stilbenes showed that substrates bind ~4–5 Å away from the metal center, allowing the solvent to remain bound to the metal without inducing major conformational changes in the protein structure (14). Comparative Mössbauer studies on NOV2, CAO1, and ACO and their respective *ES* complexes showed only minor differences in the electronic environment of the active-site Fe(II) atom, indicating small changes in iron coordination upon substrate binding to the active site (14). These observations are different from many other mononuclear nonheme iron enzymes whose iron-bound solvent molecules are displaced upon substrate binding to their active sites (17, 18). The role of the iron-coordinated solvent in O_2 binding and activation by CCDs is unclear, but a computational study on the ACO catalytic mechanism has suggested two possible scenarios (19). In the first, the solvent ligand dissociates from iron, creating a vacant site for O_2 binding. In the second, solvent ligand remains bound to iron but changes its equilibrium position to allow simultaneous binding of O_2. Here, the bound solvent could also act as a proton donor to stabilize reaction intermediates.

We sought to address the role of solvent in the alkene cleavage reaction through solvent kinetic isotope effect (sKIE) studies. Metal-bound aquo/hydroxo ligands exhibit hydrogen/deuterium fractionation factors that are less than unity ($\phi < 1$), meaning that deuterium tends to accumulate in bulk solvent as opposed to the metal-bound solvent ligand (20, 21). Thus, dissociation of the metal-bound solvent ligand is thermodynamically more favored in D_2O compared with H_2O (22). In a situation where slow aquo dissociation occurs as part of the rate-limiting step of catalysis, an inverse isotope effect is anticipated (23). Conversely, a normal KIE is expected if proton transfer occurs during a rate-limiting step of the reaction (22). These isotope effect studies were complemented with XAS and X-ray crystallography to further address O_2 gating and the proton transfer events associated with CCD catalysis. Our data on NOV2 and CAO1, respectively, indicate that the dissociation of solvent ligand from the Fe(II) ion provides the binding site for O_2, and a single proton transfer occurs during a step that is rate-limiting under some conditions. We also demonstrate that a single active-site amino acid difference between these two enzymes alters the rate-limiting step of catalysis.

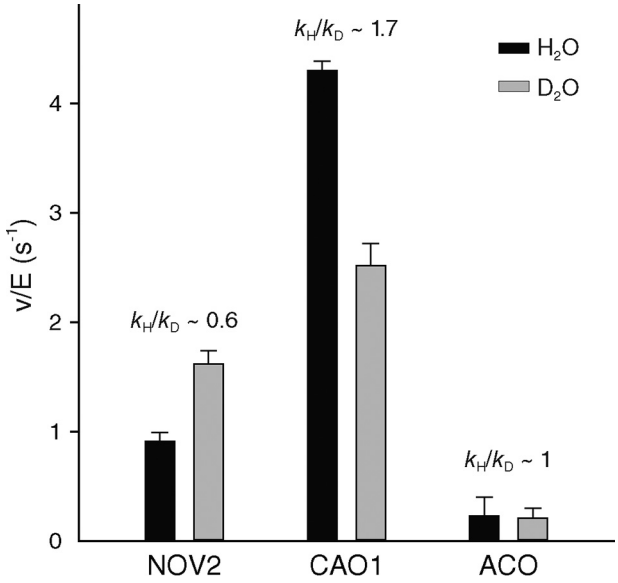

Figure 2. Solvent isotope effect on steady-state activity for NOV2, CAO1, and ACO. An inverse solvent isotope effect ($k_H/k_D \sim 0.6$), a normal kinetic isotope effect ($k_H/k_D \sim 1.7$), and no isotope effect ($k_H/k_D \sim 1$) on the apparent k_{cat} were observed for NOV2, CAO1, and ACO, respectively. Conditions used were 20 nM NOV2, CAO1, or ACO and 35 μM piceatannol for NOV2 and CAO1 or 83 μM all-*trans*-apo-8′-carotenol for ACO in HEPES buffer, pH 7.4 (pD 7.4, pH scale reading of 7.0). Mean values are shown. *Error bars* represent S.D.

Results

Three CCD enzymes each exhibit distinct isotope effects on steady-state activity

We initiated the study by measuring k_{cat} values for NOV2, CAO1, and ACO in H_2O- and D_2O-containing buffers under air-saturated conditions using standard substrates, all-*trans*-8′-apocarotenol for ACO and piceatannol for NOV2 and CAO1 (Fig. 2). The activity was monitored by optical spectrophotometry as described under "Experimental procedures" (Fig. S1) (2, 24). ACO activity was unaffected by the substitution of isotopic solvent within experimental uncertainty ($k_H/k_D = 1$). By contrast, NOV2 and CAO1 exhibited distinct kinetic behaviors in the two buffers. We observed an inverse isotope effect for NOV2 ($k_H/k_D = 0.62$), whereas CAO1 displayed a normal KIE ($k_H/k_D = 1.7$). Notably, CAO1 exhibited a significantly greater turnover number compared with NOV2 despite the reactions being carried out under identical conditions, indicating functionally important active-site differences between the two enzymes. The divergent kinetic behavior between NOV2 and CAO1 prompted us to examine their sKIE dependences in more detail.

Factors determining the inverse isotope effect on NOV2 activity

To further examine the inverse sKIE on NOV2 activity, we measured NOV2 steady-state kinetics in H_2O- and D_2O-based buffer systems at a range of substrate concentrations to allow extraction of the Michaelis–Menten kinetic parameters. We found that the inverse isotope effect on k_{cat} for NOV2 was essentially constant over the range of substrate concentrations and pL values tested under air-saturated conditions (Fig. 3). The catalytic efficiency parameter (k_{cat}/K_m), which is influ-

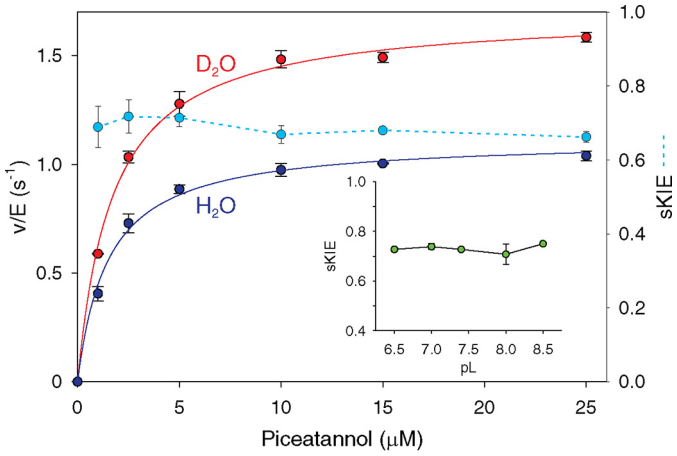

Figure 3. Solvent isotope effects on NOV2 steady-state kinetics. Shown is the solvent isotope effect on activity of NOV2 at an O_2 concentration of ~230 μM and varying substrate concentration. Substitution of H_2O with D_2O in a buffer with pH 7.4 (pD 7.4, pH scale reading of 7.0) showed an inverse isotope effect on k_{cat} (0.62 ± 0.07) and k_{cat}/K_m (0.69 ± 0.12) with a minor effect on K_m (0.90 ± 0.12), which we interpret as arising from the dissociation of water from the metal center in the process of O_2 binding. The magnitude of solvent isotope effect on k_{cat} was independent of the substrate concentration (*dashed line*), suggesting that substrate binding is uncoupled from the iron–aquo bond dissociation. The solvent isotope effect on k_{cat} was also independent of pL within the range of 6.5–8.5 (*inset*). Conditions used were 20 nM NOV2 and varying concentration (μM) of piceatannol in HEPES buffer, pH 7.4 (pD 7.4, pH scale reading of 7.0). Mean values are shown. *Error bars* represent S.D.

Table 1
Kinetic parameters for NOV2

Parameter	k_{cat}	K_m	k_{cat}/K_m
	s^{-1}	μM	$s^{-1}\cdot\mu M^{-1}$
H_2O	1.01 ± 0.08	1.54 ± 0.06	0.66 ± 0.06
D_2O	1.63 ± 0.12	1.71 ± 0.21	0.95 ± 0.14
KIE (H_2O/D_2O)	0.62 ± 0.07	0.90 ± 0.12	0.69 ± 0.12

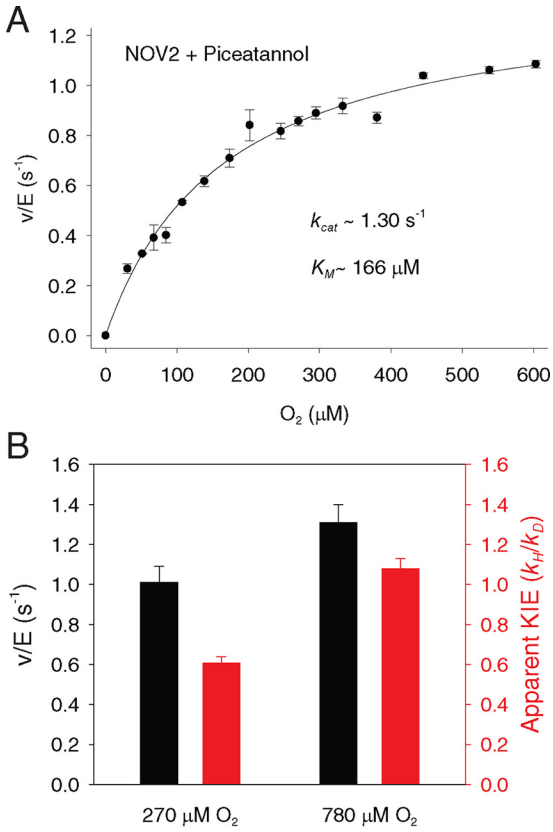

Figure 4. Dependence of NOV2 steady-state kinetics and sKIE on O_2 concentration. *A*, kinetic characterization of NOV2 at saturating substrate concentration (35 μM piceatannol) and varying O_2 concentration. NOV2 activity showed a Michaelis–Menten dependence on O_2 concentration. The kinetic parameters for NOV2 obtained from curve fitting are k_{cat} = 1.30 s^{-1} and K_m = 166 μM O_2. Conditions used were 20 nM NOV2, 35 μM piceatannol, 20 mM HEPES, pH 7.0. *B*, dependence of NOV2 activity and sKIE on O_2 concentration. Note that the sKIE was inverse at ambient O_2 concentration but became slightly normal at saturating O_2 concentration. Mean values are shown. *Error bars* represent S.D.

enced by all reaction steps up to the first irreversible step, also revealed an inverse isotope effect of approximately an equal magnitude observed for k_{cat} (Table 1).

We next asked whether the inverse isotope effect depends on the O_2 concentration in the reaction mixture. As a prerequisite to the experiment, we first determined the NOV2 steady-state kinetic parameters for O_2 at a fixed concentration of piceatannol (35 μM). We recorded k_{cat} and K_m values of 1.3 s^{-1} and 166 μM O_2, respectively, indicating that the enzyme operates at submaximal capacity in air-saturated buffer under these conditions (Fig. 4*A*). We then measured the isotope effect in O_2-saturated buffer (~780 μM O_2) in which the enzyme is fully saturated with cosubstrate and compared it with that observed in air-saturated buffer. We found that the inverse isotope effect was completely abolished under saturating O_2 conditions, suggesting a change in the rate-limiting step of the reaction (Fig. 4*B*). The observed kinetic parameters measured for NOV2 in air-saturated conditions are thus apparent parameters.

Inverse isotope effects have a limited number of documented causes in enzyme systems. These include viscosity-dependent conformational changes (25), involvement of nucleophilic thiols in catalysis (26), and aquo release from metal sites (21–23). We examined the first potential cause by carrying out reactions in an H_2O-based reaction buffer containing 9% glycerol, which matches the viscosity of a 100% D_2O-based buffer system (25). This change in viscosity resulted in a slight reduction in the reaction rate, which allowed us to rule out the first possible origin of the inverse isotope effect (Fig. S2). We excluded the second possibility as well by observing that NOV2 does not contain Cys residues at sequence positions that are predicted, based on the CAO1 crystal structure, to form its active site. Thus, the release of an aquo ligand from the metal ion best explains our inverse isotope effect observation.

Insight into the normal KIE on CAO1 catalysis

Unlike NOV2, CAO1 cleaved piceatannol in an air-saturated buffer in a mechanism that showed a normal KIE (Fig. 2). To exclude the possibility of the KIE being a result of the viscosity difference between H_2O and D_2O, we carried out the CAO1 reaction in H_2O buffer supplemented with 9% glycerol. In contrast to the results described above for NOV2, we did not observe any change in the reaction rate in the presence of glycerol (Fig. S3). We considered the possibility that the normal KIE might be a consequence of a difference in ionization behavior of side-chain residues in H_2O and D_2O. One strategy to account for such behavior is to perform the KIE studies at different pH values. We performed the CAO1 reaction at pH 6.5, 7.0, 7.4, 8.0,

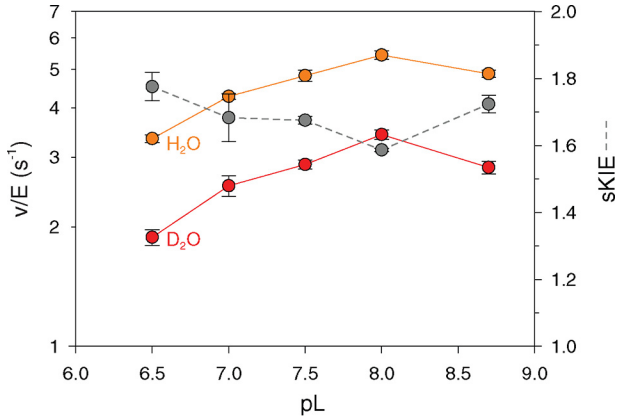

Figure 5. pH dependence of the CAO1 normal sKIE. Oxidation of piceatannol by CAO1 at ambient O_2 concentration and saturating piceatannol concentration displayed a normal kinetic isotope effect within a pL range from 6.5 to 8.7, and the magnitude of isotope effect on the apparent k_{cat} was ~1.7. Conditions used were 20 nM CAO1 and 30 μM piceatannol in HEPES buffer at varying pL. pD of D_2O was adjusted according to the pH meter reading of pH − 0.4 to match the corresponding pH of H_2O buffer. The substrate molar extinction coefficient was determined for each pL value, and the corrected values were used for the calculations. Mean values are shown. *Error bars* represent S.D. Note that the *left axis* is displayed as a $\log_{10}$ scale according to convention (40).

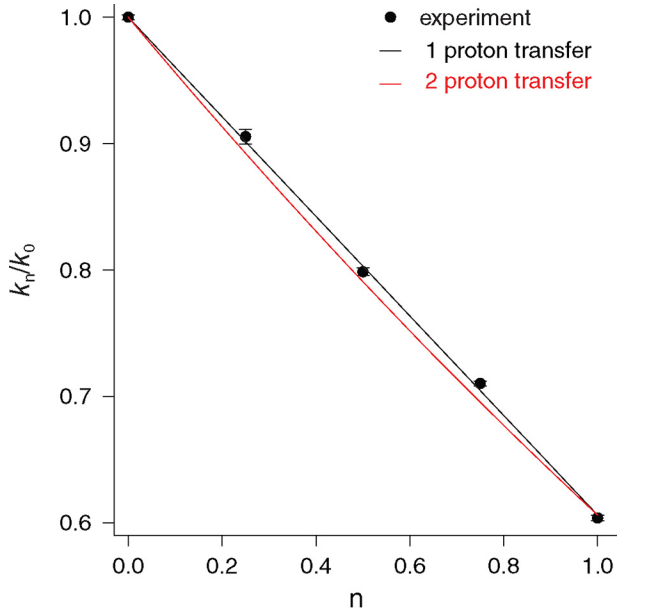

Figure 6. CAO1 proton inventory analysis. The apparent k_{cat} value at a given mole fraction of D_2O (k_n) normalized to the apparent k_{cat} in 100% H_2O-based buffer (k_0) is plotted as a function of the D_2O mole fraction (n). The plot shows a linear decrease in the turnover ratio with increasing mole fraction of D_2O. The data are best fit to the linear form of the Gross–Butler equation, which describes a single proton transfer event during the rate-limiting reaction step. By comparison, the quadratic form of the equation is plotted as a *red line* showing poorer fit to the experimental data. Conditions used were 20 nM CAO1 and 30 μM piceatannol in HEPES buffer at pH or pD 7.4. The different mole fraction of D_2O was achieved by mixing appropriate volumes of 20 mM HEPES, D_2O, pD 7.4, with 20 mM HEPES, H_2O, pH 7.4. Mean values are shown. *Error bars* represent S.D.

and 8.7 in an air-saturated buffer with saturating substrate and observed a normal KIE of similar magnitude for all pH conditions tested (Fig. 5).

Proton inventory studies probe the number of protons transferred during the transition state of the rate-limiting step (27, 28). For a normal KIE, the rate of reaction decreases with increasing mole fraction of D_2O in the reaction buffer. Such behavior was observed for CAO1 in air-saturated buffer. We plotted the ratio of the observed k_{cat} at "n" mole fraction of D_2O to k_{cat} at 100% H_2O (k_n/k_0) *versus* the mole fraction of D_2O (n) and observed a linear correlation between k_n/k_0 and n. The data from the resulting plot were fitted to the linear form of the Gross–Butler equation for a single hydron transfer with an observed KIE of ~1.7 (Fig. 6), suggesting that a single proton transfer occurred during the rate-limiting step (29).

Analogous to our experiments on NOV2, we performed isotope effect studies at varying O_2 concentrations with CAO1 to determine its effect on the KIE. We first determined the rate dependence on O_2 concentration at fixed piceatannol concentration (35 μM). The reaction rate increased in a hyperbolic manner with increasing O_2 concentration, and the data were fitted to the Michaelis–Menten equation with kinetic parameters of $k_{cat} = 4.68\ s^{-1}$ and $K_m = 114\ \mu M\ O_2$, indicating that the reaction is unsaturated for O_2 in air-saturated buffer (Fig. 7*A*). We observed that the KIE is maintained at saturating O_2 concentrations indicating that proton transfer remains rate-limiting under these conditions (Fig. 7*B*). By contrast, we observed a significant decrease in magnitude of normal KIE when the O_2 concentration was below that of air-saturated buffer, at or below its K_m value. This observation is consistent with a normal KIE competing with an inverse isotope effect.

Impact of pH changes and substrate complexation on X-ray absorption spectra of NOV2 and CAO1

Previous iron K-edge XAS analyses of NOV2 and CAO1 at pH 8.0 suggested slightly different resting-state structures for the iron centers of these enzymes, likely due to differences in exchangeable ligands such as bound solvent (14). We hypothesized that this structural difference could, at least in part, give rise to the difference in kinetic behavior between these two enzymes. To probe for pK_a differences in the primary iron-coordinating ligands between these enzymes, we performed iron K-edge XAS experiments on NOV2 and CAO1 at pH values of 6.5 and 8.5 where variations in catalytic activity could be observed (Fig. 5). K-edge X-ray absorption near-edge spectroscopy (XANES) provides information about metal coordination number, oxidation state, and electronic orbital occupancy and has been previously used to detect differences in the iron centers of CCDs (14). XANES spectra for NOV2 at pH 6.5 and 8.5 and CAO1 at pH 6.5 and 8.5 are presented in Fig. 8, *A* and *B*, respectively. The spectra are consistent with our previously published XANES data on NOV2 and CAO1, exhibiting edge inflections at 7121.7–7122.0 eV, consistent with an iron(II) formulation, as well as bimodal pre-edge absorption bands ($E_{pre\text{-}edge}$ = 7112.6 and 7114.5 eV), which are attributable to formally forbidden 1*s*-to-3*d* electronic transitions gaining intensity from admixture with 4*p* orbitals in noncentrosymmetric geometries. The shapes and intensities of the pre-edge transitions are consistent with five-coordinate iron(II) centers. Notably, we observed essentially no change in the XANES spectra between the two pH states, as evidenced by a lack of changes in the edge and pre-edge energies, and only subtle changes in pre-edge peak areas (Fig. S4 and Table S1). This result indicates that there is no change in iron-site symmetry or the effective

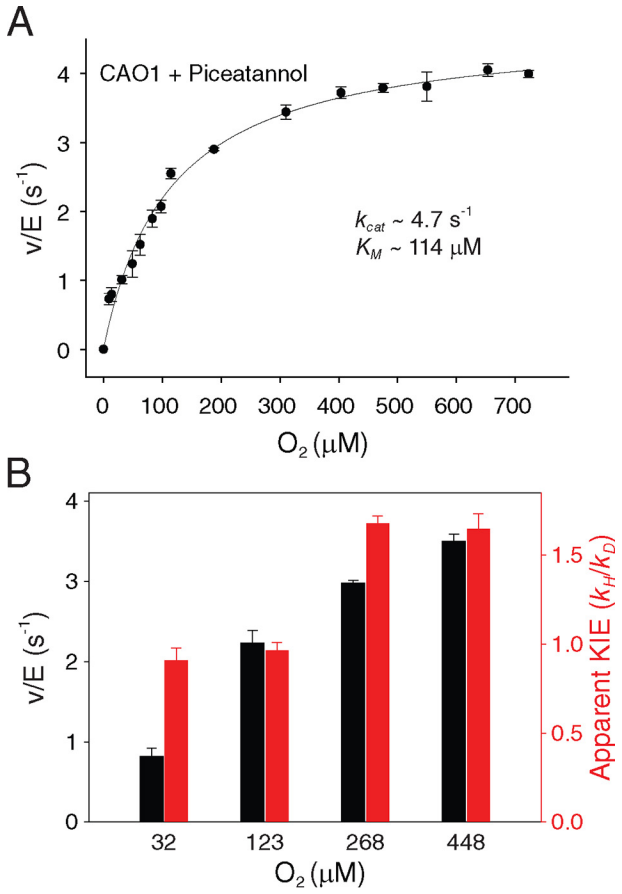

Figure 7. Dependence of CAO1 steady-state kinetics and isotope effect on O_2 concentration. *A*, kinetic characterization of CAO1 at saturating substrate concentration (30 μM piceatannol) and varying O_2 concentration. CAO1 activity showed a Michaelis–Menten dependence on O_2 concentration. The kinetic parameters for CAO1 obtained from curve fitting are k_{cat} = 4.7 s^{-1} and K_m = 114 μM O_2. *B*, CAO1 activity and apparent sKIE as a function of O_2 concentration. A normal isotope effect was observed at ambient and enriched O_2 concentrations but vanished at concentrations below ambient levels. Conditions used were 20 nM CAO1 and 30 μM piceatannol in HEPES buffer at varying pL. pD of D_2O was adjusted according to the pH meter reading of pH − 0.4 to match the corresponding pH of H_2O buffer. Mean values are shown. *Error bars* represent S.D.

nuclear charge experienced by the iron(II) center. We therefore suggest that there is no change in iron coordination environment over this pH range and that ligands in the iron primary coordination sphere have pK_a values outside the pH range studied here.

Although NOV2 and CAO1 crystallographic and Mössbauer spectroscopy studies have indicated that solvent remains bound to iron in the presence of organic substrate (14), we considered the possibility that substrate binding may weaken the metal–aquo bond in CAO1 more so than in NOV2, thus altering the rate-limiting step. To test this hypothesis, we undertook XANES studies of enzyme (*E*) and *ES* complexes of NOV2 and CAO1 at pH 7.4 (Fig. 8, *C* and *D*, respectively). Binding of piceatannol to NOV2 and CAO1 afforded a small ~0.2-eV increase in edge energies for the *ES* states relative to their *E*-only counterparts as well as a slight reduction in white line intensity. The former suggests that the iron environment became slightly more electropositive in the presence of piceatannol (Fig. S5 and Table S2), whereas the latter suggests a possible subtle increase in the distribution of bond lengths seen by the iron(II) center in both NOV2 and CAO1. However, the 1*s*-to-3*d* pre-edge peak positions and areas changed only subtly between the two states, suggesting that substrate binding does not elicit a significant change in iron coordination environment for either NOV2 or CAO1.

A single amino acid substitution converts CAO1 solvent isotope effect from normal to inverse

The apparent lack of differential pH and substrate-binding effects on the iron environments of NOV2 and CAO1 prompted us to directly examine structural differences between these enzymes that could underlie their different behaviors in isotopic solvents. Crystallization conditions have previously been established for CAO1 (14), whereas NOV2 has proven recalcitrant to crystallization. Therefore, we focused on CAO1 for crystallographic analysis. Considering the apparent difference in stability of the iron–solvent complex between the two enzymes suggested by the kinetic isotope effects, we inspected the Fe–CAO1 crystal structure (14) for residues in proximity to this moiety (*i.e.* within 8 Å) (Fig. 9*A*) and compared these with homologous sites in NOV2 (Fig. 9*B*). From this comparison, we identified three sites differing between CAO1 and NOV2, namely amino acid positions 91, 383, and 509. To investigate the impact of these differences on the isotope effect, we generated F91L, E383D, and L509V point mutants of CAO1 and examined their activity in H_2O- and D_2O-based buffers. We observed that the normal KIE was maintained in both the F91L and E383D variants, whereas an inverse isotope effect, similar in magnitude to that of NOV2, was observed for L509V CAO1 (Fig. 9*C*). Inspection of the CAO1 structure revealed that, aside from the iron-coordinating His residues, the L509 $C^{\delta 2}$ atom makes the closest van der Waals interaction with the coordinated aquo ligand. Such a close contact would be altered by substitution of a Val side chain at position 509, which suggested that this difference could influence the strength of solvent interaction with iron. To gain further insights into the mechanism of this effect, we crystallized L509V and WT CAO1 under similar conditions and determined their structures by X-ray diffraction analysis (Table 2).

The overall structure of L509V CAO1 was similar to that of the WT protein with an average root-mean-square difference of ~0.15 Å between chains in equivalent positions within the asymmetric unit. The presence of a Val residue at position 509 was fully supported by the difference electron density map calculated after the first cycle of refinement with Leu modeled at the site (Fig. S6). Refinement of the updated L509V model against the data resulted in an excellent fit of the Val side chain to the density. Interestingly, Val-509 adopted a conformation within the outlier region of the Val/Ile-specific Ramachandran plot, although its ϕ-ψ angles reside in an allowed region of corresponding general plot (30). The only other notable active site difference between the two proteins was found at Phe-91 where the side chain adopted an alternative conformation with its phenyl ring rotated away from the iron center nestled within a hydrophobic cavity formed by Pro-89, Trp-340, Trp-339, and Tyr-133 side chains (Fig. S7). The alteration was possibly triggered by a loss of long-range van der Waals contacts normally formed between the Phe-91 and Leu-509 side chains. Nearly

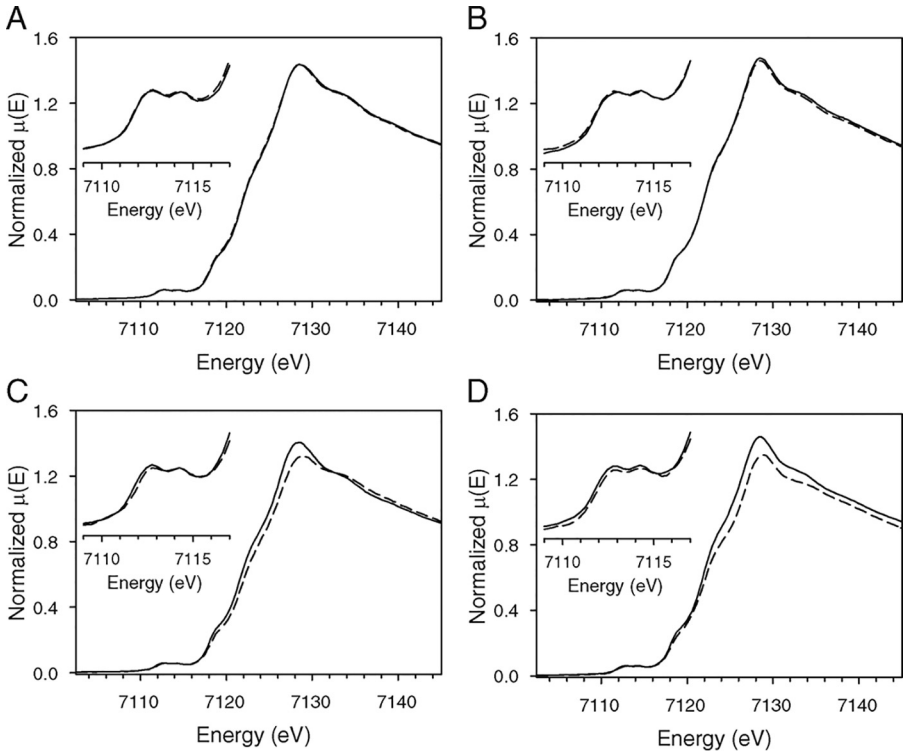

Figure 8. Iron K-edge XAS analysis of NOV2 and CAO1. Normalized XANES spectra of as-isolated NOV2 at pH 6.0 (*solid lines*) and pH 8.5 (*dashed lines*) (*A*), as-isolated CAO1 at pH 6.0 (*solid lines*) and pH 8.5 (*dashed lines*) (*B*), as-isolated (*solid lines*) and *ES* (*dashed lines*) states of NOV2 at pH 7.4 (*C*), and as-isolated (*solid lines*) and *ES* (*dashed lines*) states of CAO1 at pH 7.4 (*D*). μ(*E*), absorption coefficient.

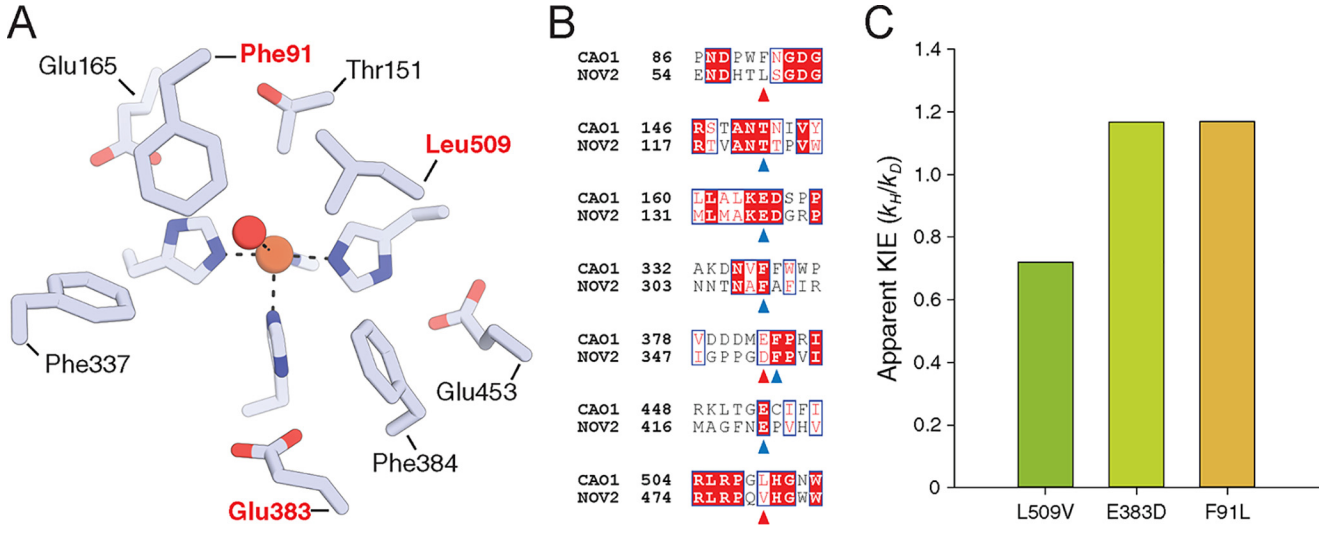

Figure 9. Active-site variation between CAO1 and NOV2 and impact of amino acid substitutions on CAO1 sKIEs. *A*, residues within 8 Å of the CAO1 metal center are shown as *sticks*. Those labeled in *bold red* text are sites differing between CAO1 and NOV2. Iron and water are shown as *brown* and *red spheres*, respectively. *B*, selected regions of an amino acid sequence alignment between CAO1 and NOV2 that are centered on the residues labeled in *A* (marked by *arrows* under the sequence alignment). Three residues close to the iron center are nonidentical between CAO1 and NOV2 (marked with *red arrows*). *C*, substitution of Leu-509 with Val, as found in NOV2, changes the KIE from normal to inverse, whereas the other two active-site substitutions preserve the normal sKIE as observed for piceatannol cleavage by wild-type CAO1. The experimental conditions were similar to that of Fig. 5. Mean values are shown for *C*.

identical active-site structural differences were observed in a second L509V CAO1 crystal structure obtained under distinct crystallization conditions (Fig. S8 and Table S2). The extent to which this induced structural difference applies to NOV2 is unclear given that the protein contains a different residue at the corresponding sequence position (Leu instead of Phe; Fig. 9*B*). The overall result of the L509V substitution in CAO1 is thus an expansion of the active-site volume available for ligand binding within the iron coordination site *trans* to His-197.

Inspection of the difference electron density maps revealed an alteration in appearance between the WT and L509V CAO1 structures (Fig. 10). In our previously reported WT CAO1 structure (14), a relatively weak density was present near the iron center *trans* to His-197 that we modeled as a bound solvent

Table 2
X-ray diffraction data collection and structure refinement statistics
r.m.s., root-mean-square.

Data collection and processing			
Crystal	L509V CAO1[a] (condition 1)	L509V CAO1[a] (condition 2)	WT CAO1
X-ray source	APS 24-ID-E	NSLS-II 17-ID-2	APS 24-ID-E
Wavelength (Å)	0.97918	0.979339	0.97918
Space group	$P3_221$	$P3_221$	$P3_221$
Unit cell lengths (Å)	$a = 101.21, c = 450.18$	$a = 99.55, c = 447.49$	$a = 101.31, c = 449.20$
Resolution (Å)[b]	50–2.15 (2.28–2.15)	50–1.95 (2.07–1.95)	50–2.04 (2.16–2.04)
Unique reflections	146,769 (23,282)	188,611 (30,515)	168,673 (24,186)
Multiplicity	12.9 (13.3)	20.6 (19.4)	10.4 (8.7)
Completeness (%)	99.9 (99.7)	100 (99.9)	97.9 (87.9)
$\langle I/\sigma I \rangle$	10 (1.2)	12.7 (1.4)	13.6 (1.1)
$R_{merge}I$ (%)	17 (253.5)	16.1 (290)	13.9 (168.1)
$CC_{1/2}$ (%)[c]	99.8 (53.5)	99.9 (76.5)	99.8 (49.2)
Wilson *B*-factor (Å^2)	52	44	42
Refinement			
Resolution (Å)[b]	49.4–2.15 (2.21–2.15)	49.5–1.95 (2.00–1.95)	49.4–2.04 (2.09–2.04)
No. reflections[d]	140,279 (6,490)	179,182 (9,429)	161,048 (7,569)
R_{work}/R_{free} (%)[b]	19.8/21.8 (36.4/34.7)	18.7/20.5 (34.2/35.3)	18.1/21.1 (38.8/40.5)
No. atoms	16,707	16,739	17,068
Protein	15,969	15,829	15,925
Iron	4	4	4
Water	730	902	1,135
⟨*B*-factor⟩ (Å^2)	56.2	49.0	41.5
Protein	56.4	49.0	41.5
Iron	46.0	39.3	57.9
Water	51.2	50.8	41.9
r.m.s. deviations			
Bond lengths (Å)	0.004	0.007	0.008
Bond angles (°)	1.23	1.35	1.42
Ramachandran plot (% favored/outliers)[e]	97.6/0.4	97.4/0.2	97.3/0
MolProbity score (%)	100	100	100
PDB accession code	6N1Y	6N20	6N21

[a] Data from two isomorphous crystals were merged to produce the final data set.
[b] Values in parentheses are for the highest-resolution shell of data.
[c] $CC_{1/2}$ is the correlation coefficient between half-sets of the data.
[d] Values in parentheses are the number of reflections used for cross-validation.
[e] Evaluated using MolProbity.

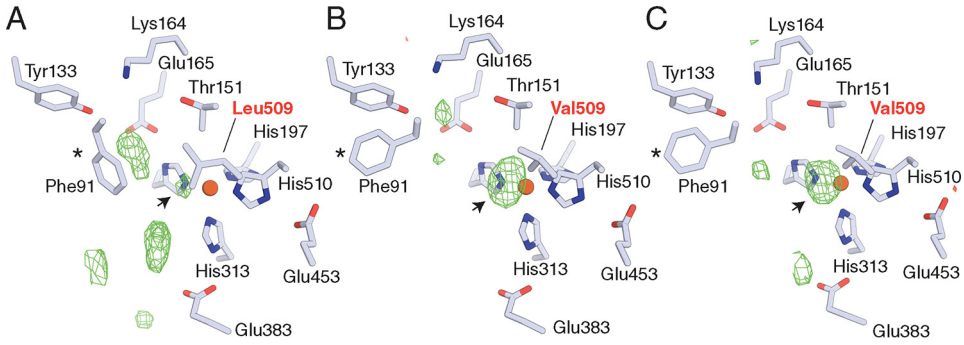

Figure 10. Structural alterations induced by an L509V substitution in CAO1. *A*, WT CAO1 crystal. *B*, L509V CAO1 crystal grown under conditions similar to the WT structure shown in *A*. *C*, L509V CAO1 crystal grown under alternative conditions. *Green* and *red mesh* represents σA-weighted $F_o - F_c$ electron density contoured at +5 and −5 root-mean-square deviation, respectively. Note the difference in electron density appearance near the iron center (indicated by *arrows*) and the change in Phe-91 conformation in the L509V structures (marked by *asterisks*). The structures shown in each panel are from equivalent protomers of the respective asymmetric units such that the crystal-packing environments are similar. Active-site structures for all four chains of the asymmetric units of the three crystal structures are shown in Fig. S8. Data collection and refinement statistics for each structure are shown in Table 2.

molecule. We obtained a similar result with WT CAO1 in the present study but found that one protomer of the asymmetric unit (Fig. S8, chain C) had a particularly low difference electron density at this position, making the iron appear four-coordinate. This observation is notable given that the four-coordinate state of the Fe(II) center is likely the one capable of binding and reacting with O_2. By contrast, both L509V structures featured stronger and larger difference electron density peaks at the corresponding coordination position. The density was heterogeneous when comparing different chains, which confounded our ability to assign it to a particular ligand. Attempts to model a single solvent molecule into the density resulted in reasonable iron–solvent bond lengths and *B*-factors but did not satisfactorily quench all of the difference density at the site. The addition of a second scatterer in the form of an O_2 molecule accounted for more of the difference electron density, but the refined O_2 ligand was found in a variety of orientations and distances contrary to chemical expectations. In light of the structural alterations described above for L509V that reduce hydrophobicity near the iron center and increase the potential ligand-binding volume, it is conceivable that the density represents multiple solvent ligands, each with partial occupancy.

It is notable that although the iron and surrounding $N^{\epsilon 2}$ atoms of the coordinating His residues had atomic *B*-factors of

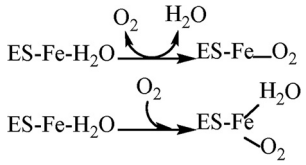

Scheme 1. Possible fates of the iron-coordinated solvent in CCDs.

similar magnitude, indicative of full iron occupancy, the WT CAO1 iron *B*-factors were disproportionately higher, suggesting either static or dynamic heterogeneity and/or incomplete occupancy (Table 2). The apparent stronger ligand coordination observed for L509V CAO1 may help restrain the iron mobility and potentially prevent its dissociation, which would account for the lower iron *B*-factors.

Discussion

The steady-state kinetic isotope effects observed for NOV2, CAO1, and ACO when the protic solvent (H_2O) is substituted by its isotope (D_2O) provide an opportunity to gain insights into the different steps of CCD catalysis. Previous computational results suggested two different mechanisms for O_2 binding. In the first, the aquo ligand dissociates from the Fe center and provides the binding site for O_2, whereas in the second, water remains bound to iron but changes its equilibrium position to accommodate O_2 binding as shown in Scheme 1.

Our results for NOV2 under air-saturated conditions support a mechanism in which the aquo ligand dissociates during O_2 binding/activation. In air-saturated buffer (~280 μM O_2), NOV2 demonstrated an inverse isotope effect on the steady-state k_{cat} ($k_H/k_D = 0.61$), which measures the rate-limiting step of the overall reaction. Based on previously measured inverse fractionation factors ($\phi < 1$) for metal-bound aquo ligands (20) and experimental evidence of an inverse isotope effect reflecting metal–aquo dissociation in hypoxia-inducible factor–prolyl hydroxylase (23), we assigned the origin of the inverse isotope effect on NOV2 k_{cat} to slow dissociation of metal-bound aquo ligand during catalysis. Due to the $\phi < 1$, the dissociation of D_2O ligand is thermodynamically more favorable than the dissociation of H_2O ligand, thus increasing the probability of O_2 binding to the iron center, resulting in an inverse equilibrium isotope effect on the steady-state activity. This observation establishes that for NOV2, and possibly for all CCDs, the dissociation of aquo ligand occurs during or prior to O_2 binding/activation. The isotope effect on the steady-state k_{cat} also suggests that aquo ligand rebinds during or after each catalytic cycle to reset the system for the next round of catalysis. Finally, the isotope effect on another kinetic parameter, k_{cat}/K_m (sKIE = 0.69), with a magnitude similar to that observed for k_{cat}, further suggests that the dissociation of aquo ligand occurs prior to the first irreversible step.

Although NOV2 and CAO1 both catalyze oxidation of piceatannol, unlike NOV2, we observed a normal kinetic isotope effect on CAO1 steady-state activity ($k_H/k_D = 1.7$) in an air-saturated buffer. The corresponding proton inventory demonstrated that a single proton transfer occurred in the transition state of the rate-limiting step for this enzyme. The normal KIE of approximately equal magnitude at different pH values for CAO1 demonstrates that the isotope effect is a consequence of proton transfer occurring in a chemical step rather than being associated with a difference in side-chain ionization in the two buffers. It was previously suggested that proton transfer could occur from the 4-hydroxyl stilbenoid group to side-chain proton acceptors to generate an activated substrate intermediate (14, 15). In fact, crystal structures of CAO1 in complex with piceatannol or β-fluororesveratrol feature a short hydrogen bond (~2.45–2.55 Å) formed between the stilbenoid 4-hydroxyl group and the Tyr-133 hydroxyl group, suggesting the formation of a moderately strong hydrogen bond. Lys amine groups located in the protein interior, like that of Lys-166, can have dramatically downshifted pK_a values, enabling them to act as proton acceptors at near neutral pH values (31). Based on these considerations, it is possible that deuterium substitution at the stilbenoid 4-hydroxyl group and consequent elevated pK_a could underlie the normal sKIE observed for CAO1. However, a pure effect on substrate pK_a is inconsistent with the enzyme activity shown in Fig. 5, where the pH-activity data are vertically downshifted in D_2O- *versus* H_2O-based solvent rather than being shifted to the right as would be expected for a pure effect on the hydroxyl group acidity. This mechanism also does not account for the O_2 dependence of the KIE.

Alternatively, proton transfer could also occur from an iron-bound solvent molecule or an unidentified proton donor to an activated oxygen species, allowing its temporary stabilization. Studies on other mononuclear nonheme iron enzymes demonstrate that proton transfer to activated oxygen species and reaction intermediates is critical in governing their reaction trajectories (Ref. 32 and references therein). The possibility of such a proton transfer event occurring in CCDs was suggested by prior density functional theory studies on apocarotenoid cleavage by ACO (19) and is consistent with the kinetic data we present here.

These experimental results and structural considerations indicate that the iron-bound solvent plays a crucial role in the catalytic mechanism of CCDs. Previous extended X-ray absorption fine structure data indicated that the iron-bound solvent moiety is found in an aquo state in NOV2, whereas CAO1 exhibited scattering consistent with the presence of both hydroxo and aquo ligands (14). Conversely, the XAS edge position of CAO1 is slightly blue-shifted with respect to that of NOV2, indicating a more electropositive character (less surrounding negative charge) of the iron center of the former protein (14). Our XAS studies on NOV2 and CAO1 with varying pH (6.5–8.5) indicated no alteration in the primary ligand environment of the iron center, whereas deprotonation of an Fe(II)–aquo complex would be expected to detectably alter the XAS spectrum (23). Thus, it appears that the protonation states of the first-sphere iron ligands in these CCDs remain unchanged within a pH range of 6.5–8.5. For both NOV2 and CAO1, substrate complexation did result in a subtle perturbation in the XANES spectrum, but the alteration is likely too small to be attributable to induced dissociation of the solvent molecule. This conclusion is also supported by prior ^{57}Fe Mössbauer spectroscopy experiments, which showed only minor spectral changes upon organic substrate complexation by NOV2 and CAO1 (14). Indeed, crystal structures of Co–CAO1, which is structurally similar to Fe–CAO1 (33), in complex with

piceatannol demonstrate that solvent can remain bound to metal in the presence of substrate.

Our mutagenesis studies showing that KIE behavior in CAO1 can be inverted by a single substitution from Leu to Val at position 509 also support the importance of the iron–solvent unit in the catalytic mechanism of CCDs. This position contains one of the few active-site differences between CAO1 and NOV2. The Leu-509 side chain is located in close proximity to the iron-bound solvent in WT CAO1 and is predicted to interact with the aquo ligand through van der Waals interactions. The structure of L509V CAO1 demonstrates that this substitution changes the orientation of aliphatic side-chain contact with the solvent-binding site but leaves the remaining active-site structure mostly unchanged with the exception of Phe-91, which was found in a new conformation pointing away from the iron-coordinated solvent. This combination of structural changes produced an opening in the exchangeable ligand-binding site, allowing greater ligand accessibility as evidenced by the much stronger difference electron density near the iron center compared with that for WT CAO1. The L509V CAO1 density was heterogeneous, having a variable appearance in different monomers of the asymmetric unit. Although we could not assign the density to a particular molecule, its strength suggests tighter binding of ligands, including solvent, to the L509V CAO1 iron center. Such an effect could explain the inverse sKIE we observed for L509V CAO1 and, by implication, NOV2 as deuterium substitution favors dissociation of the iron–solvent bond, providing an energetically more favorable path to the transition state. Although this explanation is compelling, we cannot exclude other influences as factors responsible for the change in sKIE behavior, including changes in substrate-binding orientation. However, the extra density observed in L509V CAO1 supports the idea that the smaller Val side chain allows more room for ligand binding, such as the interaction of additional solvent molecules to the metal-coordinated aquo ligand.

The overall activity of WT CAO1, having an apparently weaker iron–solvent interaction, is not limited by a slow solvent dissociation step in the catalytic cycle, and the effects of solvent deuterium substitution manifest instead on a chemical proton transfer step, giving rise to a normal KIE. In summary, we conclude that the dissociation of solvent bound to iron and proton transfer are two chemical steps associated with the catalytic mechanism of CCDs.

Experimental procedures

Reagents and protein purification

All the chemicals used in enzyme purification and enzymatic assays were purchased from Sigma-Aldrich. LB medium was purchased from USB (Cleveland, OH). All chemicals were used without any further purification. Water from a Milli-Q purification system (resistivity of 18.2 megohm-cm) (ED Millipore, Billerica, MA) was used to prepare all reagents and buffer solutions. NOV2 protein was expressed in *Escherichia coli* and purified as described previously (2). The purity of the isolated protein (>95%) was established visually by SDS-PAGE followed by Coomassie Blue staining. The concentration of protein was quantified using a molar extinction coefficient of 69,786 M^{-1} cm^{-1} at $\lambda_{280\ nm}$ (14). ACO from *Synechocystis* sp. PCC6803 and CAO1 from *Neurospora crassa* were also purified as described previously (14, 34). The variants of CAO1 (L509V, E383D, and F91L) were generated using a standard site-directed mutagenesis protocol. CAO1 L509V was purified following the protocol described for WT CAO1.

Activity assay

4-[(*E*)-2-(3,5-Dihydroxyphenyl)ethenyl]benzene-1,2-diol, also known as piceatannol (Sigma-Aldrich), was used as a substrate for NOV2 and CAO1. The rate of piceatannol oxidation was monitored with a UV-visible spectrophotometer (PerkinElmer Life Sciences, Lambda Bio+) by following the change in absorbance at 304 nm over time. The decrease in absorbance at 304 nm corresponds to the steady-state rate of piceatannol oxidation. All the assays were performed at room temperature (21–23 °C) in a reaction buffer consisting of 20 mM HEPES-NaOH, pH 7.4. ACO activity assays were carried out using all-*trans*-8′-apocarotenol as a substrate as described previously (24).

The O_2 concentration dependence study was performed inside an AtmosBag (Sigma-Aldrich). The partial pressure of O_2 inside the bag was modulated by supplying an appropriate mixture of N_2 and O_2 gases using a customized gas mixer (Superflash, Cleveland, OH). The buffer consisting of 20 mM HEPES-NaOH, pH 7.4, was allowed to equilibrate with the atmosphere of the bag for 15 min with gentle stirring. Afterward, the concentration of dissolved O_2 was measured using an RDO optical dissolved O_2 sensor (Thermo Scientific, Waltham, MA). The O_2 sensor was calibrated according to manufacturer guidelines using air-saturated water. Once a stable O_2 concentration was recorded, 1 ml of the buffer was transferred to a 1.5-ml cuvette (BrandTech Scientific, Germany). An appropriate amount of piceatannol was added from a 2 mM stock prepared in 20 mM HEPES-NaOH, pH 7.2. The mixture was used to blank the UV-visible spectrometer. 20 nM NOV2 or CAO1 was finally added to initiate the reaction. The reaction was monitored by following the decrease in substrate absorbance at 304 nm. This procedure was repeated at various concentrations of O_2.

Solvent isotope effect

20 mM HEPES buffer was prepared in H_2O and D_2O (99.9% D). The pH/pD of these corresponding buffers was adjusted to 7.4. pD 7.4 was obtained by adjusting the pH meter reading to 7.0 ($pD = pH_{read} + 0.4$). 4 M NaOH was used to make the pH adjustments. Piceatannol stock was made in H_2O and D_2O separately in 20 mM HEPES-NaOH, and the pH/pD was adjusted to 7.4. The experiments were carried out exactly as described in the preceding section. For the D_2O experiment, 2 μM NOV2 or CAO1 stock was prepared in 20 mM HEPES, D_2O buffer, pD 7.4, and the mixture was allowed to stand at room temperature for about 30 min before using it for activity assays. The final percentage of D in the D_2O buffer was about 98–99%. All solvent isotope effect reaction measurements were performed either under air or inside an AtmosBag as specified in the figure legends.

Solvent viscosity assay

Steady-state assays under ambient O_2 concentration were performed in 9% glycerol in H_2O buffer to mimic the viscosity difference between H_2O and D_2O.

XAS sample preparation and data collection

The resting-state *E*-only samples at pH 7.4, 6.0, and 8.5 were prepared in atmospheric air by mixing NOV2 or CAO1 in 100 mM buffer (50 mM HEPES and 50 mM MES) with 20% glycerol (v/v). Approximately 30 min after mixing, 140 μl of this mixture was transferred to the sample holder and flash frozen in liquid nitrogen. The *ES* complex samples were prepared under an argon atmosphere inside a glove bag to prevent any catalytic turnover. NOV2 or CAO1 (~1 mM) was mixed with piceatannol (~2 mM) in 20 mM HEPES, pH 7.4, containing 20% glycerol (v/v). The mixtures were transferred to the sample holder using a gas-tight syringe and flash frozen in liquid nitrogen. The *E*/*ES* complex and pH profile XAS data for NOV2 and CAO1 were collected on Stanford Synchrotron Radiation Lightsource (SSRL) 9-3 and 7-3, respectively, following previously described methods (14). The inflection point of the iron foil reference was set to 7112.0 eV. All XAS data processing and analysis were done according to the previously established protocol for CCDs (14).

Effect of pH on isotope effect

10 mM HEPES (pK_a = 7.5) and 10 mM MES (pK_a = 6.15) were used as a cobuffer system to create assay solutions at pH (pD) values of 6.5, 7.0, 7.5, 8.0, and 8.75. The molar extinction coefficient for piceatannol was measured for each pH (pD), and the calculated value was used to process the data.

Proton inventory

Solvent deuterium kinetic isotope effect experiments were performed for CAO1 by mixing 20 mM HEPES buffer in D_2O or H_2O (pD or pH, 7.4). A subtle difference in the molar extinction coefficient of piceatannol was observed for different mole fraction of D_2O. The corrected molar absorption coefficient was used for the calculation. The activity (apparent k_{cat} denoted as k_n) measured at a given mole fraction of D_2O was divided by the apparent k_{cat} in 100% H_2O (k_0), and the ratio was plotted against the mole fraction of D_2O (n). The plot was fit to the Gross–Butler equation for a single proton transfer (21),

$$k_n/k_0 = 1 - n + a \times n \quad \text{(Eq. 1)}$$

where n is the mole fraction of D_2O and a = 1/KIE.

Protein crystallization, diffraction data collection, and structure refinement

L509V CAO1 protein (~35 mg/ml) and WT CAO1 (~40 mg/ml) were crystallized by the hanging-drop vapor-diffusion method in a crystallization mixture containing 33% (w/v) poly(acrylic acid 2100 sodium salt) and 28% (w/v) poly(acrylic acid 2100 sodium salt), respectively, with 0.1 M HEPES-NaOH, pH 6.0. The crystal quality was improved by introducing nucleating microseeds from a previously grown crystal of WT CAO1 in 43% (w/v) poly(acrylic acid sodium salt) and 0.1 M HEPES, pH 6.0. L509V CAO1 was also crystallized using a second crystallization mixture consisting of 100 mM imidazole/MES, pH 6.5, 30 mM $MgCl_2$, 30 mM $CaCl_2$, 10% (w/v) PEG 20,000, and 20% (v/v) PEG monomethyl ether 550. Rod-shaped crystals grew in about 1 week and were harvested after ~5–6 weeks. The isolated crystals were flash frozen directly in liquid nitrogen without the addition of any further cryoprotectant. The harvested crystals were stored in liquid nitrogen prior to X-ray exposure. Diffraction data were collected from N_2-vapor cooled crystals at the Northeastern Collaborative Access Team (NE-CAT) beamline 24-IDE of the Advanced Photon Source or the FMX beamline (17-ID-2) at the National Synchrotron Light Source-II. Diffraction data were processed with XDS and XSCALE (35). Initial phases were obtained either by direct refinement or by molecular replacement using Phaser (36) and the atomic coordinates of a previously determined Fe–CAO1 structure (PDB accession code 5U8X) as an initial model. The structures were refined and manually edited using REFMAC (37) and Coot (38) and validated using the MolProbity (30) and wwPDB servers (39). In all cases, the N terminus of CAO1 was disordered and consequentially omitted from the model. Additionally, residues 335–351 in chain B of the second crystal form of L509V CAO1 were partially disordered and omitted from the final model.

Author contributions—N. K., E. R. F., and P. D. K. conceptualization; N. K., E. R. F., H. E. H., W. S., J. v. L., and P. D. K. formal analysis; N. K. and P. D. K. writing-original draft; N. K. and P. D. K. writing-review and editing; W. S. and J. v. L. methodology; P. D. K. funding acquisition.

Acknowledgments—This work is based in part upon research conducted at the Advanced Photon Source Northeastern Collaborative Access Team beamline 24ID-E supported by National Institutes of Health (NIH) Grants GM103403 and RR029205 and United States Department of Energy (DOE) Contract DE-AC02-06CH11357. Use of SSRL beamlines 7-3 and 9-3 was made possible by the United States DOE Office of Science under Contract DE-AC02-76SF00515 to SLAC National Accelerator Laboratory and NIH Grant P41-GM-103393 (SSRL Structural Molecular Biology Program). Data for this study were measured at beamline 17-ID-2 (FMX) of the National Synchrotron Light Source-II, which is supported by NIH Grant GM111244 and DOE Office of Biological and Environmental Research Grant KP1605010. The NSLS-II is supported in part by the DOE Office of Science, Office of Basic Energy Sciences Program under Contract DE-SC0012704 (Grant KC0401040). The Case Center for Synchrotron Biosciences is supported by NIH Grant EB009998.

References

1. Sui, X., Kiser, P. D., and von Lintig, J., and Palczewski, K. (2013) Structural basis of carotenoid cleavage: from bacteria to mammals. *Arch. Biochem. Biophys.* **539,** 203–213 CrossRef Medline
2. Sui, X., Golczak, M., Zhang, J., Kleinberg, K. A., von Lintig, J., Palczewski, K., and Kiser, P. D. (2015) Utilization of dioxygen by carotenoid cleavage oxygenases. *J. Biol. Chem.* **290,** 30212–30223 CrossRef Medline
3. Kloer, D. P., and Schulz, G. E. (2006) Structural and biological aspects of carotenoid cleavage. *Cell. Mol. Life Sci.* **63,** 2291–2303 CrossRef Medline
4. Kamoda, S., and Saburi, Y. (1993) Cloning, expression, and sequence analysis of a lignostilbene-α,β-dioxygenase gene from *Pseudomonas paucimobilis* TMY1009. *Biosci. Biotechnol. Biochem.* **57,** 926–930 CrossRef Medline

5. Giuliano, G., Al-Babili, S., and von Lintig, J. (2003) Carotenoid oxygenases: cleave it or leave it. *Trends Plant Sci.* **8,** 145–149 CrossRef Medline
6. Wyss, A. (2004) Carotene oxygenases: a new family of double bond cleavage enzymes. *J. Nutr.* **134,** 246S–250S CrossRef Medline
7. Scherzinger, D., Ruch, S., Kloer, D. P., Wilde, A., and Al-Babili, S. (2006) Retinal is formed from apo-carotenoids in *Nostoc* sp. PCC7120: *in vitro* characterization of an apo-carotenoid oxygenase. *Biochem. J.* **398,** 361–369 CrossRef Medline
8. Schwartz, S. H., Tan, B. C., Gage, D. A., Zeevaart, J. A., and McCarty, D. R. (1997) Specific oxidative cleavage of carotenoids by VP14 of maize. *Science* **276,** 1872–1874 CrossRef Medline
9. Moise, A. R., von Lintig, J., and Palczewski, K. (2005) Related enzymes solve evolutionarily recurrent problems in the metabolism of carotenoids. *Trends Plant Sci.* **10,** 178–186 CrossRef Medline
10. Al-Babili, S., and Bouwmeester, H. J. (2015) Strigolactones, a novel carotenoid-derived plant hormone. *Annu. Rev. Plant Biol.* **66,** 161–186 CrossRef Medline
11. Lobo, G. P., Isken, A., Hoff, S., Babino, D., and von Lintig, J. (2012) BCDO2 acts as a carotenoid scavenger and gatekeeper for the mitochondrial apoptotic pathway. *Development* **139,** 2966–2977 CrossRef Medline
12. Kloer, D. P., Ruch, S., Al-Babili, S., Beyer, P., and Schulz, G. E. (2005) The structure of a retinal-forming carotenoid oxygenase. *Science* **308,** 267–269 CrossRef Medline
13. Messing, S. A., Gabelli, S. B., Echeverria, I., Vogel, J. T., Guan, J. C., Tan, B. C., Klee, H. J., McCarty, D. R., and Amzel, L. M. (2010) Structural insights into maize viviparous14, a key enzyme in the biosynthesis of the phytohormone abscisic acid. *Plant Cell* **22,** 2970–2980 CrossRef Medline
14. Sui, X., Weitz, A. C., Farquhar, E. R., Badiee, M., Banerjee, S., von Lintig, J., Tochtrop, G. P., Palczewski, K., Hendrich, M. P., and Kiser, P. D. (2017) Structure and spectroscopy of alkene-cleaving dioxygenases containing an atypically coordinated non-heme iron center. *Biochemistry* **56,** 2836–2852 CrossRef Medline
15. McAndrew, R. P., Sathitsuksanoh, N., Mbughuni, M. M., Heins, R. A., Pereira, J. H., George, A., Sale, K. L., Fox, B. G., Simmons, B. A., and Adams, P. D. (2016) Structure and mechanism of NOV1, a resveratrol-cleaving dioxygenase. *Proc. Natl. Acad. Sci. U.S.A.* **113,** 14324–14329 CrossRef Medline
16. Loewen, P. C., Switala, J., Wells, J. P., Huang, F., Zara, A. T., Allingham, J. S., and Loewen, M. C. (2018) Structure and function of a lignostilbene-α,β-dioxygenase orthologue from *Pseudomonas brassicacearum*. *BMC Biochem.* **19,** 8 CrossRef Medline
17. Costas, M., Mehn, M. P., Jensen, M. P., and Que, L., Jr. (2004) Dioxygen activation at mononuclear nonheme iron active sites: enzymes, models, and intermediates. *Chem. Rev.* **104,** 939–986 CrossRef Medline
18. Neidig, M. L., and Solomon, E. I. (2005) Structure-function correlations in oxygen activating non-heme iron enzymes. *Chem. Commun.* 5843–5863 CrossRef Medline
19. Borowski, T., Blomberg, M. R., and Siegbahn, P. E. (2008) Reaction mechanism of apocarotenoid oxygenase (ACO): a DFT study. *Chemistry* **14,** 2264–2276 CrossRef Medline
20. Kassebaum, J. W., and Silverman, D. N. (1989) Hydrogen-deuterium fractionation factors of the aqueous ligand of cobalt in $Co(H_2O)_6^{2+}$ and Co(II)-substituted carbonic anhydrase. *J. Am. Chem. Soc.* **111,** 2691–2696 CrossRef
21. Quinn, D. M., and Sutton, L. D. (1991) Theoretical basis and mechanistic utility of solvent isotope effects, in *Enzyme Mechanism from Isotope Effects* (Cook, P. F., ed) pp. 73–126, CRC Press, Boca Raton, FL
22. Schowen, K. B., and Schowen, R. L. (1982) Solvent isotope effects on enzyme systems. *Methods Enzymol.* **87,** 551–606 CrossRef Medline
23. Flagg, S. C., Giri, N., Pektas, S., Maroney, M. J., and Knapp, M. J. (2012) Inverse solvent isotope effects demonstrate slow aquo release from hypoxia inducible factor-prolyl hydroxylase (PHD2). *Biochemistry* **51,** 6654–6666 CrossRef Medline
24. Choi, E. H., Suh, S., Sander, C. L., Hernandez, C. J. O., Bulman, E. R., Khadka, N., Dong, Z., Shi, W., Palczewski, K., and Kiser, P. D. (2018) Insights into the pathogenesis of dominant retinitis pigmentosa associated with a D477G mutation in RPE65. *Hum. Mol. Genet.* **27,** 2225–2243 CrossRef Medline
25. Karsten, W. E., Lai, C. J., and Cook, P. F. (1995) Inverse solvent isotope effects in the NAD-malic enzyme reaction are the result of the viscosity difference between D_2O and H_2O—implications for solvent isotope effect studies. *J. Am. Chem. Soc.* **117,** 5914–5918 CrossRef
26. Weiss, P. M., Cook, P. F., Hermes, J. D., and Cleland, W. W. (1987) Evidence from nitrogen-15 and solvent deuterium isotope effects on the chemical mechanism of adenosine deaminase. *Biochemistry* **26,** 7378–7384 CrossRef Medline
27. Venkatasubban, K. S., and Schowen, R. L. (1984) The proton inventory technique. *CRC Crit. Rev. Biochem.* **17,** 1–44 CrossRef Medline
28. Kohen Amnon and Limbach Hans-Heinrich. (2006) *Isotope Effects in Chemistry and Biology*, pp. 995–1018, Taylor & Francis, Boca Raton, FL
29. Khadka, N., Milton, R. D., Shaw, S., Lukoyanov, D., Dean, D. R., Minteer, S. D., Raugei, S., Hoffman, B. M., and Seefeldt, L. C. (2017) Mechanism of nitrogenase H_2 formation by metal-hydride protonation probed by mediated electrocatalysis and H/D isotope effects. *J. Am. Chem. Soc.* **139,** 13518–13524 CrossRef Medline
30. Williams, C. J., Headd, J. J., Moriarty, N. W., Prisant, M. G., Videau, L. L., Deis, L. N., Verma, V., Keedy, D. A., Hintze, B. J., Chen, V. B., Jain, S., Lewis, S. M., Arendall, W. B., 3rd, Snoeyink, J., Adams, P. D., *et al.* (2018) MolProbity: more and better reference data for improved all-atom structure validation. *Protein Sci.* **27,** 293–315 CrossRef Medline
31. Isom, D. G., Castañeda, C. A., Cannon, B. R., and García-Moreno, B. (2011) Large shifts in pK_a values of lysine residues buried inside a protein. *Proc. Natl. Acad. Sci. U.S.A.* **108,** 5260–5265 CrossRef Medline
32. Sutherlin, K. D., Wasada-Tsutsui, Y., Mbughuni, M. M., Rogers, M. S., Park, K., Liu, L. V., Kwak, Y., Srnec, M., Böttger, L. H., Frenette, M., Yoda, Y., Kobayashi, Y., Kurokuzu, M., Saito, M., Seto, M., *et al.* (2018) Nuclear resonance vibrational spectroscopy definition of O_2 intermediates in an extradiol dioxygenase: correlation to crystallography and reactivity. *J. Am. Chem. Soc.* **140,** 16495–16513 CrossRef Medline
33. Sui, X., Farquhar, E. R., Hill, H. E., von Lintig, J., Shi, W., and Kiser, P. D. (2018) Preparation and characterization of metal-substituted carotenoid cleavage oxygenases. *J. Biol. Inorg. Chem.* **23,** 887–901 CrossRef Medline
34. Sui, X., Kiser, P. D., Che, T., Carey, P. R., Golczak, M., Shi, W., von Lintig, J., and Palczewski, K. (2014) Analysis of carotenoid isomerase activity in a prototypical carotenoid cleavage enzyme, apocarotenoid oxygenase (ACO). *J. Biol. Chem.* **289,** 12286–12299 CrossRef Medline
35. Kabsch, W. (2010) XDS. *Acta Crystallogr. D Biol. Crystallogr.* **66,** 125–132 CrossRef Medline
36. McCoy, A. J., Grosse-Kunstleve, R. W., Adams, P. D., Winn, M. D., Storoni, L. C., and Read, R. J. (2007) Phaser crystallographic software. *J. Appl. Crystallogr.* **40,** 658–674 CrossRef Medline
37. Murshudov, G. N., Skubák, P., Lebedev, A. A., Pannu, N. S., Steiner, R. A., Nicholls, R. A., Winn, M. D., Long, F., and Vagin, A. A. (2011) REFMAC5 for the refinement of macromolecular crystal structures. *Acta Crystallogr. D Biol. Crystallogr.* **67,** 355–367 CrossRef Medline
38. Emsley, P., Lohkamp, B., Scott, W. G., and Cowtan, K. (2010) Features and development of Coot. *Acta Crystallogr. D Biol. Crystallogr.* **66,** 486–501 CrossRef Medline
39. Read, R. J., Adams, P. D., Arendall, W. B., 3rd, Brunger, A. T., Emsley, P., Joosten, R. P., Kleywegt, G. J., Krissinel, E. B., Lütteke, T., Otwinowski, Z., Perrakis, A., Richardson, J. S., Sheffler, W. H., Smith, J. L., Tickle, I. J., *et al.* (2011) A new generation of crystallographic validation tools for the protein data bank. *Structure* **19,** 1395–1412 CrossRef Medline
40. Gadda, G., and Fitzpatrick, P. F. (2013) Solvent isotope and viscosity effects on the steady-state kinetics of the flavoprotein nitroalkane oxidase. *FEBS Lett.* **587,** 2785–2789 CrossRef Medline